Supplementary Information (SI) for Physical Chemistry Chemical Physics.


# Revealing the $N_2$ gas-Induced Gate-Opening in Mn-ZIF-8 and Cu-ZIF-8 from the Perspective of *In Situ* EPR Spectroscopy.

Antareekshya Deka[1], Muhammad Fernadi Lukman[1], Sibo Chetry[2], Christian Jänke[2], Harald Krautscheid[2] and Andreas Pöppl[1]*

[1] *Felix Bloch Institute for Solid State Physics, Leipzig University, 04103 Leipzig, Germany*
[2] *Institute of Inorganic Chemistry and Crystallography, Leipzig University, 04103 Leipzig, Germany*

* *Corresponding author, e-mail address: poeppl@physik.uni-leipzig.de*

## Supplementary Information

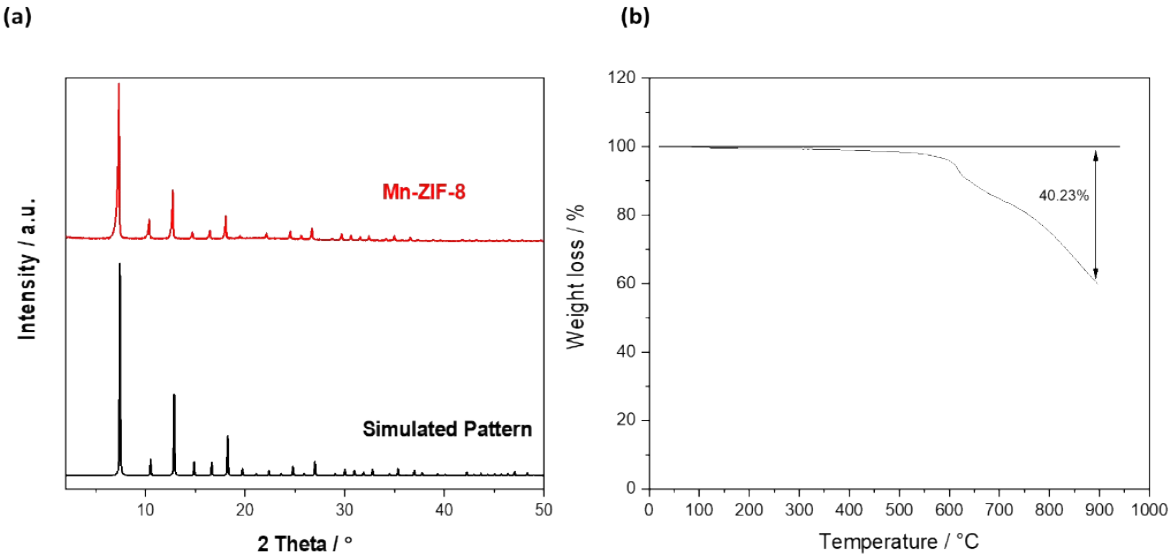


Figure S1. (a) PXRD data of Mn-ZIF-8 (red,λ = 1.54060 Å) and simulated pattern of ZIF-8 (black) (b) TGA profile of Mn-ZIF-8.

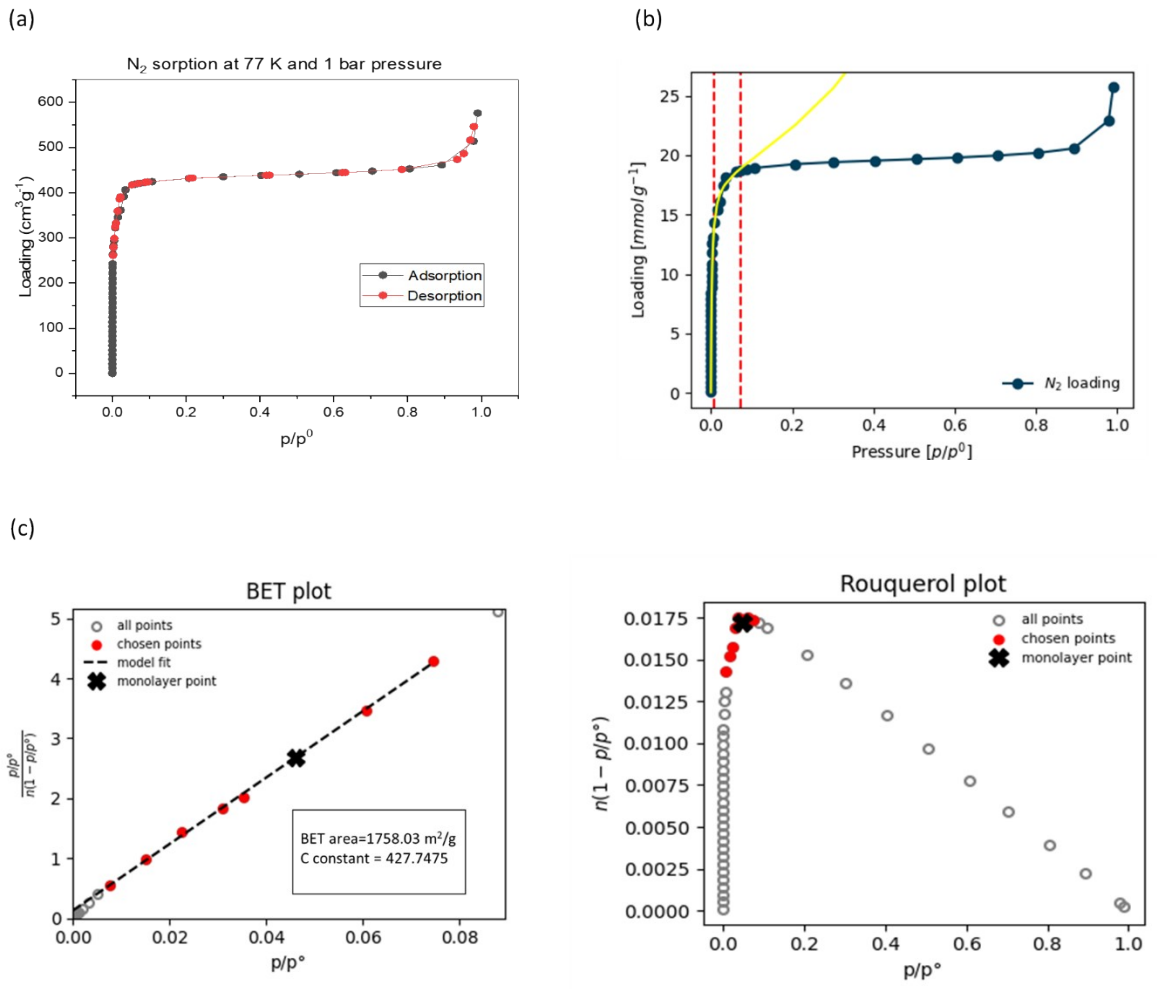


Figure S2. (a) $N_2$ sorption isotherm of Mn-ZIF-8, (b) $N_2$ adsorption branch taken for BET area calculation, (c) BET plot and (d) Rouquerol plot.

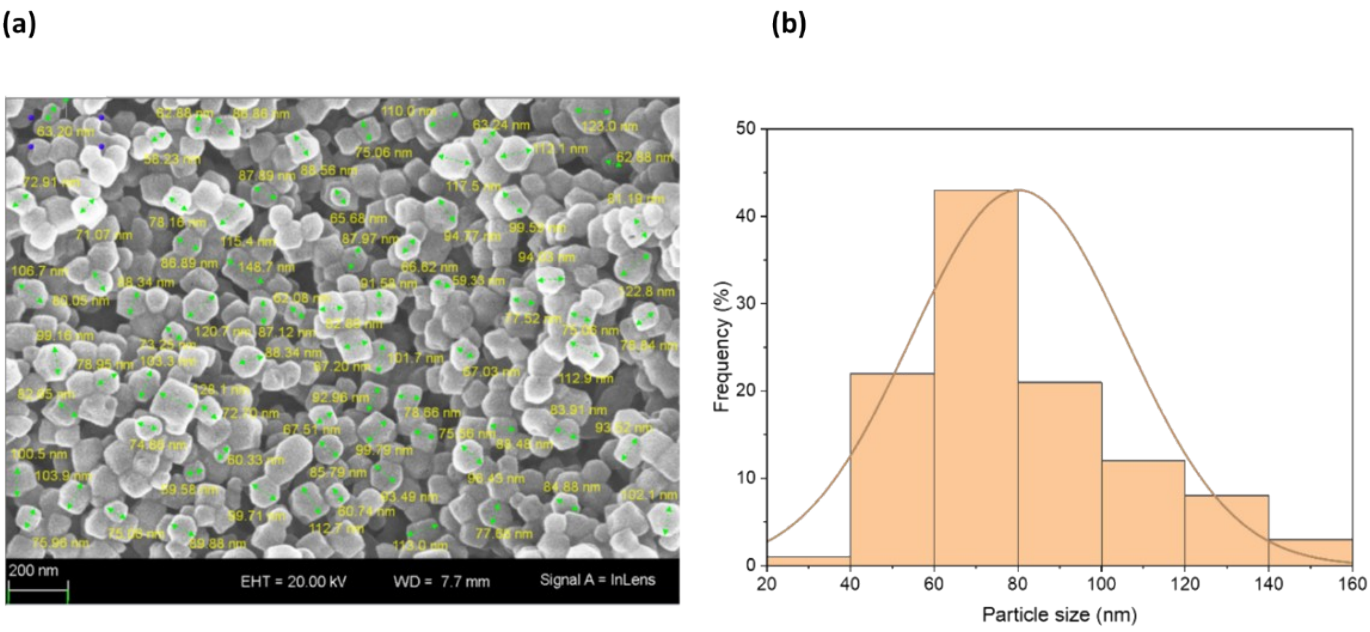


Figure S3. (a) SEM image of Mn-ZIF-8, (b) particle size distribution.

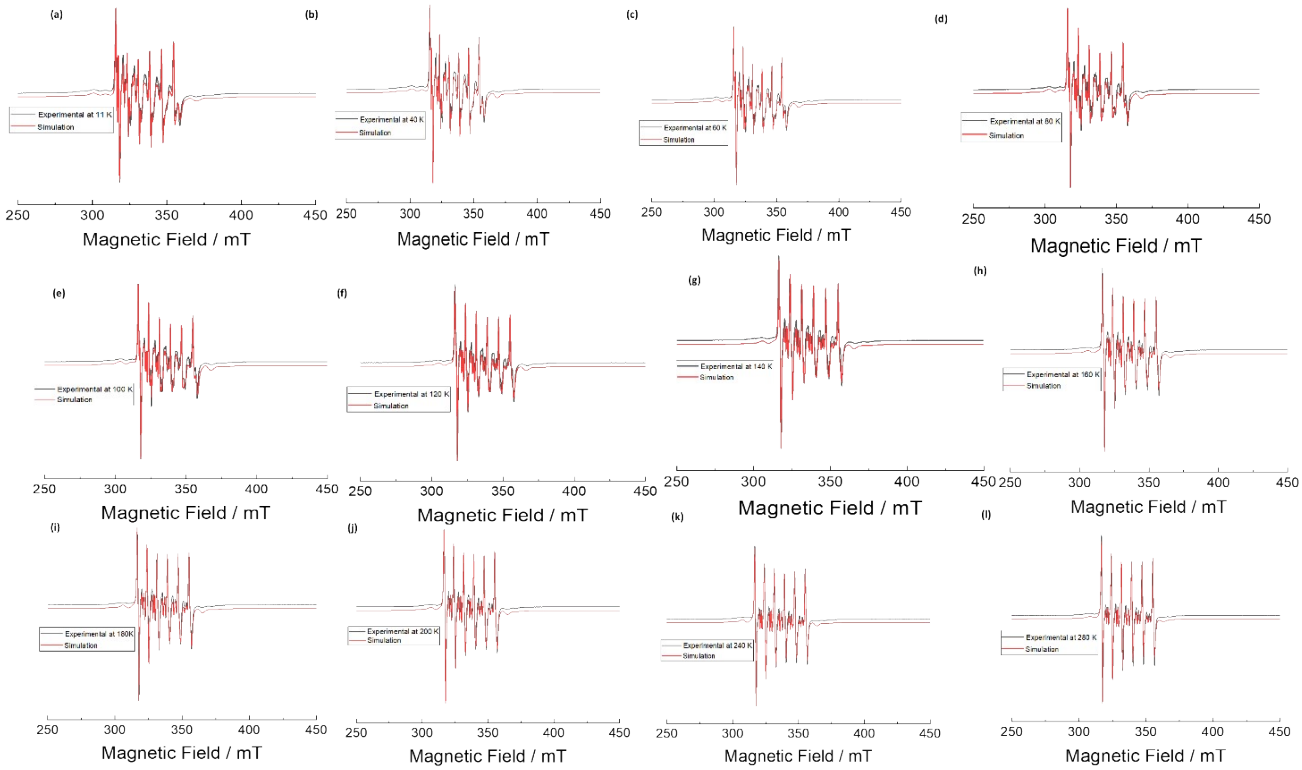


Figure S4. Spectral simulation (red) and experimental (black) X-band CW EPR spectra of Mn-ZIF-8 at different temperatures.

Table S1. Simulated EPR parameters of Mn-ZIF-8 at different temperatures. Room temperature and *T*= 20 K simulated spectra are shown in Figures 2(a) and 3(a), respectively. The first linewidth represents the Gaussian linewidth and the second linewidth represents the Lorentzian linewidth.

| Temperature (K) | *g* (MHz) | *A* (MHz) | *D* (MHz) | *E* (MHz) | $\boldsymbol{\Delta} D$ (MHz) | Linewidth (mT) |
|---|---|---|---|---|---|---|
| 11 | 1.9987(2) | -217(1) | 390(10) | 20(2) | 135(5) | 0.30,0.43 |
| 40 | 2.0001(3) | -217(1) | 370(10) | 10(2) | 140(5) | 0,0.52 |
| 60 | 2.0005(2) | -217(1) | 350(10) | 10(2) | 140(10) | 0.10,0.60 |
| 80 | 2.0005(3) | -217(1) | 330(5) | 0 | 140(10) | 0,0.45 |
| 100 | 1.9983(1) | -217(1) | 325(5) | 0 | 140(5) | 0,0.65 |
| 120 | 1.9987(2) | -217(1) | 290(10) | 0 | 135(5) | 0,0.67 |
| 140 | 1.9985(1) | -217(1) | 270(10) | 0 | 130(5) | 0,0.70 |
| 160 | 1.9985(1) | -217(1) | 265(5) | 0 | 130(5) | 0,0.68 |
| 180 | 1.9985(1) | -217(1) | 260(5) | 0 | 120(5) | 0,0.75 |
| 200 | 1.9988(1) | -217(1) | 250(10) | 0 | 130(5) | 0,0.75 |
| 240 | 1.9988(1) | -217(1) | 230(10) | 0 | 110(10) | 0,0.75 |
| 280 | 1.9988(1) | -217(1) | 205(10) | 0 | 150(10) | 0,0.75 |

The temperature dependence of the $Mn^{2+}$ ZFS parameter *D* is a common phenomenon for solid-state system [1,2] and has been described in terms of (I) the thermal contraction of the lattice [3] or (II) lattice vibrations coupled to the $Mn^{2+}$ centre[2] .In case of (I) the phenomenological expression

$$D(T) = D_0\left(1 + A\,T^n\right) \quad (1)$$

did not provide a satisfactory fit to the experimental data *D*(*T*).

Assuming mechanism (II) with [1,2]:

$$D(T) = D_0 + \delta \coth\left(h\nu/2k_BT\right) \quad (2)$$

where $\nu$ is the phonon frequency and $k_B$ the Boltzmann constant, the fitting parameters

$D_0 = 395\ MHz\ \pm 0.613\ MHz$

$$\nu\ = (2.01 \pm 0.000754)X10^9\ s^{-1}$$

$$\delta = (-0.034 \pm 0.000629)\ MHz$$

provide a reasonable fit to the experimental data. We can only speculate that in that case an internal, thermally excited, motion within the $MnN_4$ tetrahedra with such a characteristic frequency might lead to the observed temperature dependence of *D*.

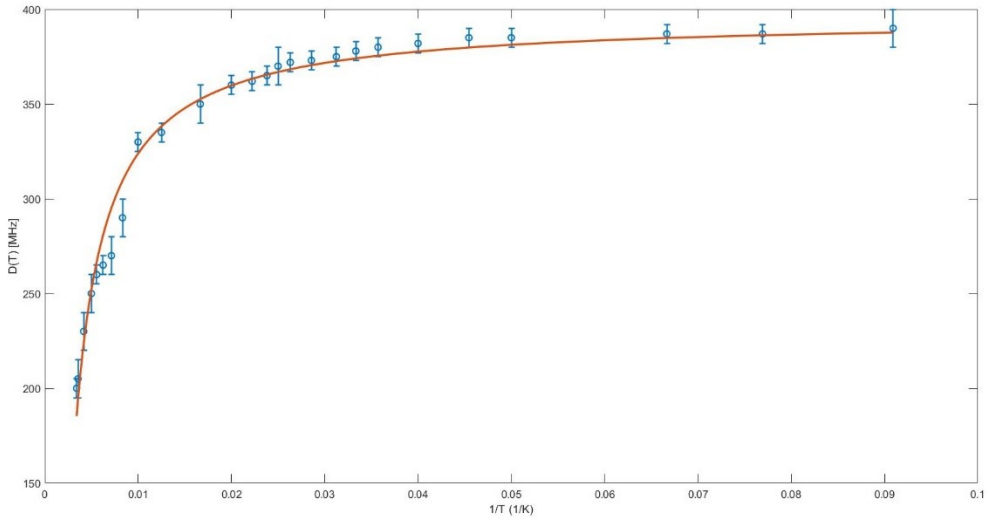


Figure S5. Zero-field splitting parameter *D* of Mn-ZIF-8 decreases with increasing temperature.

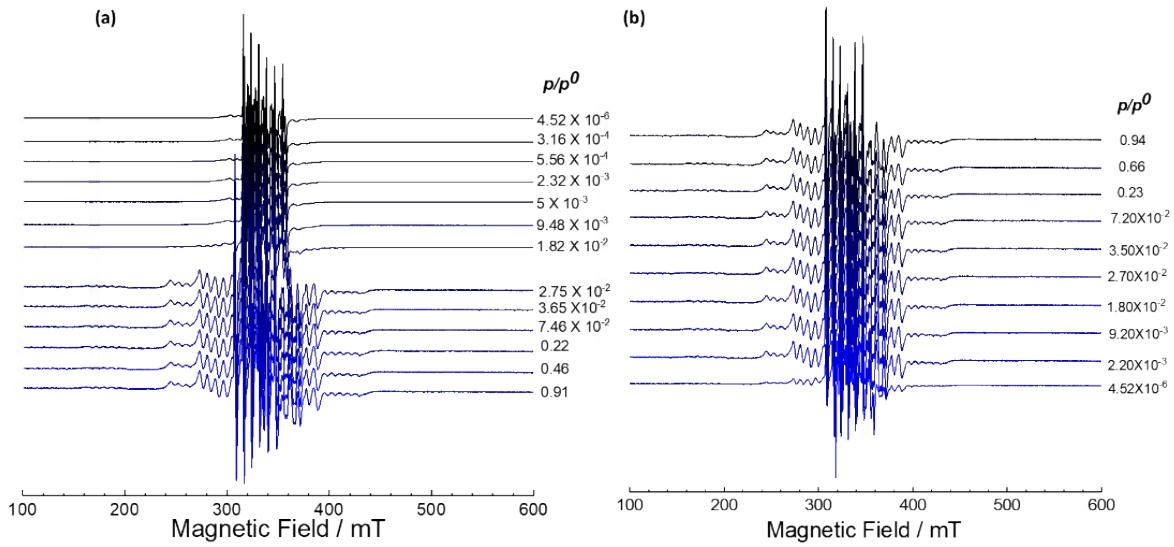

Figure S6. *In situ* X- band EPR spectra of Mn-ZIF-8 during (a) $N_2$ adsorption and (b) $N_2$ desorption at various pressures.

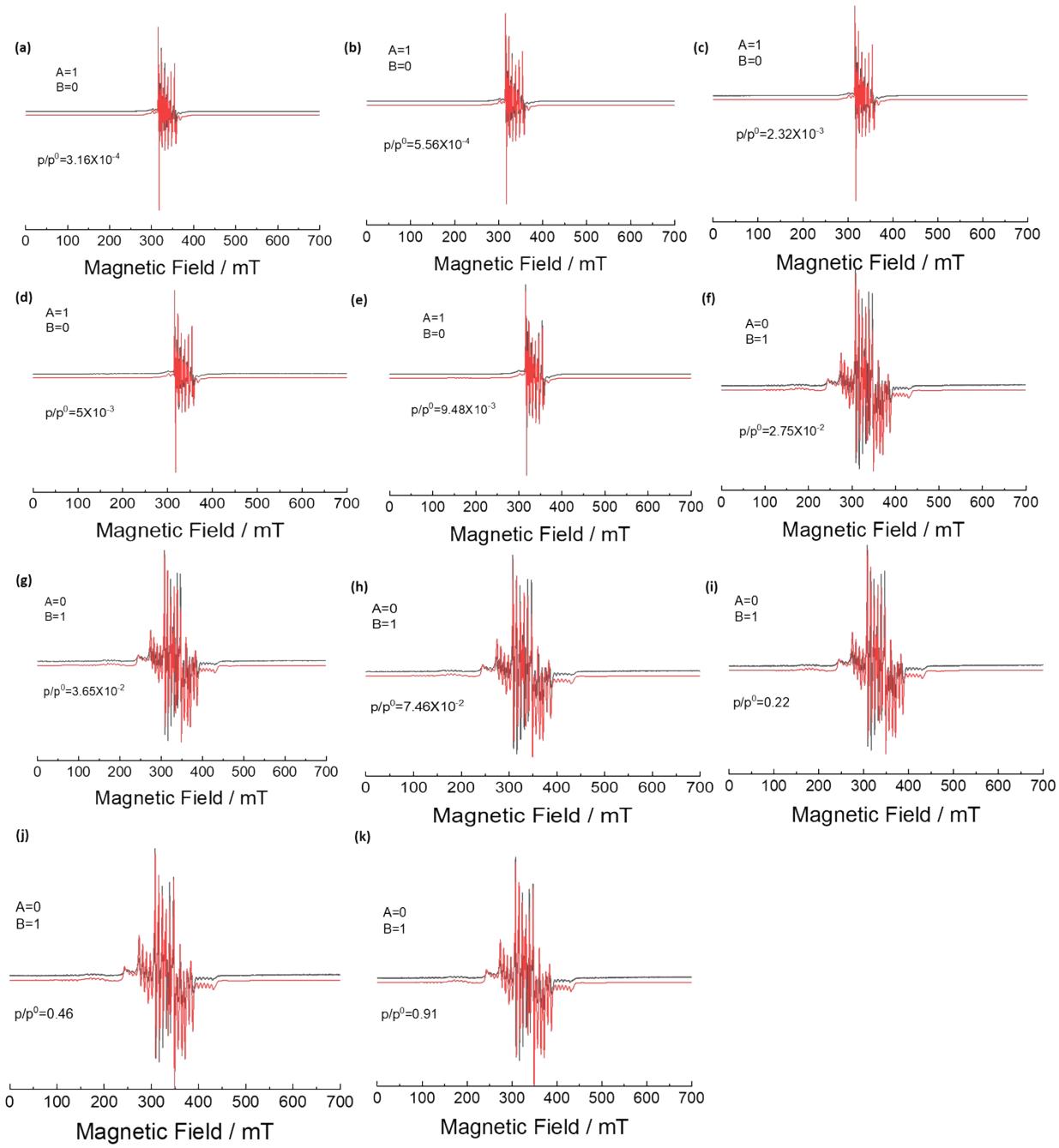


Figure S7. Experimental(black) and simulated(red) *in situ* EPR spectra of Mn-ZIF-8 during $N_2$ adsorption stages and their corresponding simulations.

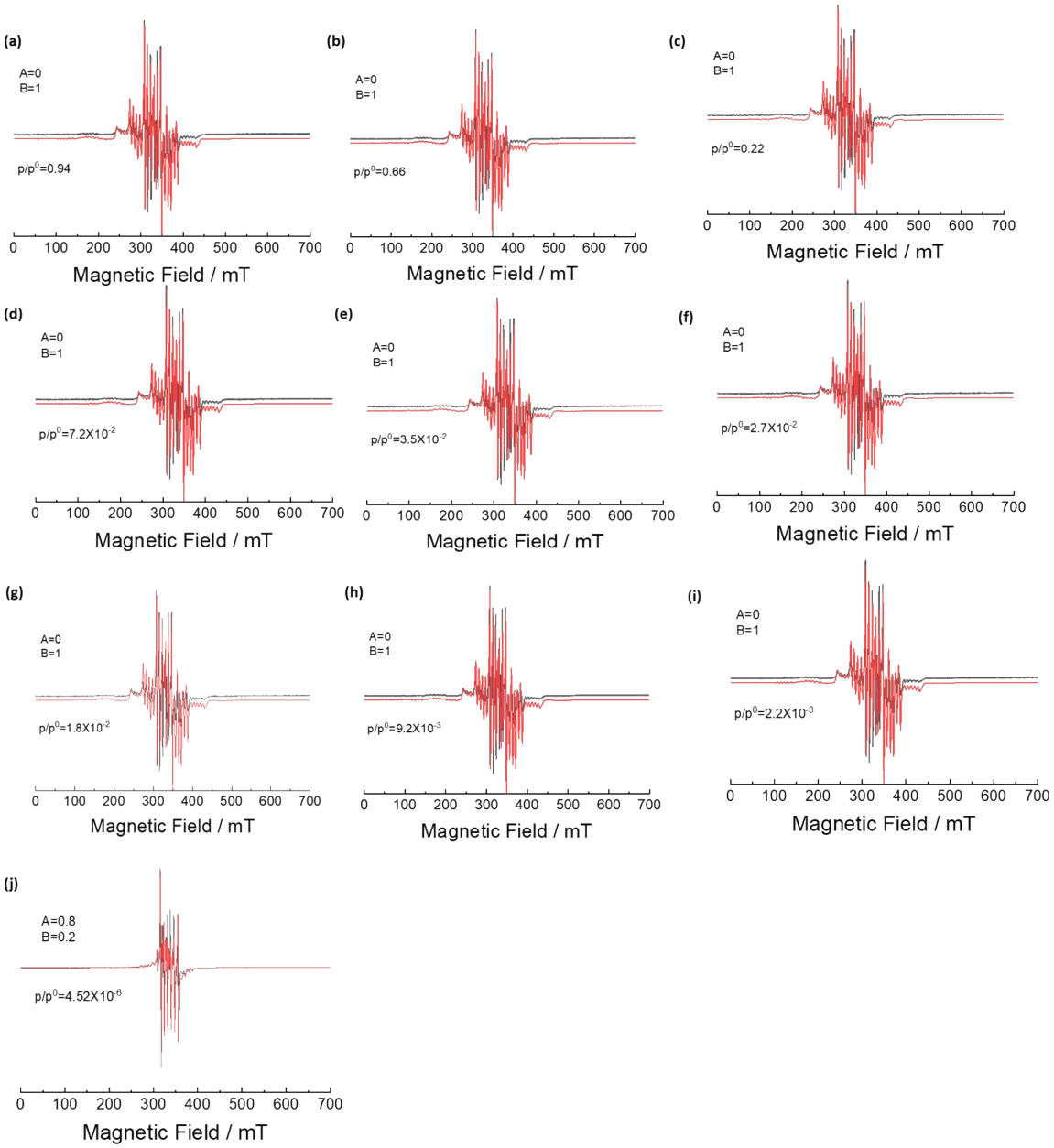


Figure S8. Experimental(black) and simulated(red) *in situ* EPR spectra of Mn-ZIF-8 during $N_2$ desorption stages and their corresponding simulations.

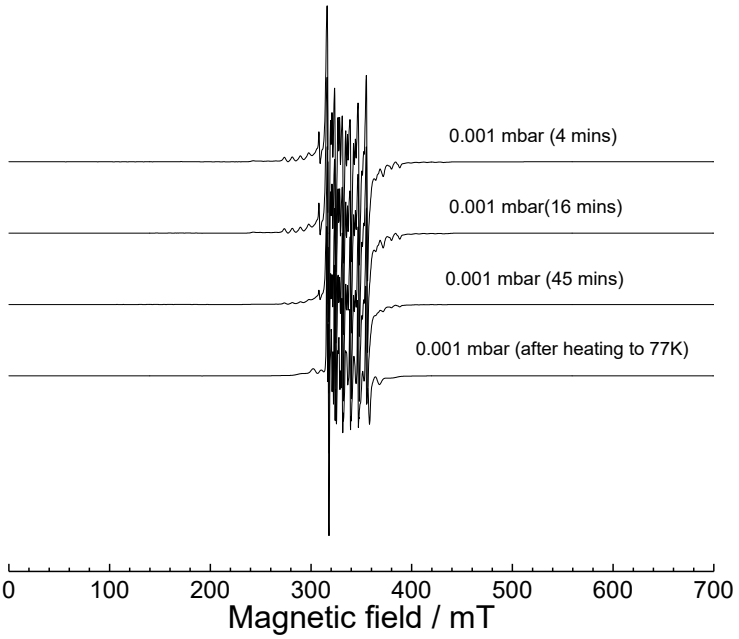


Figure S9. *In situ* EPR spectra of Mn-ZIF-8 during $N_2$ desorption recorded under varying waiting times at pressure 0.001 mbar ($p/p^0$=4.52x10$^{-6}$ mbar) and at T= 66 K, followed by heating to T=77 K at the final pressure.

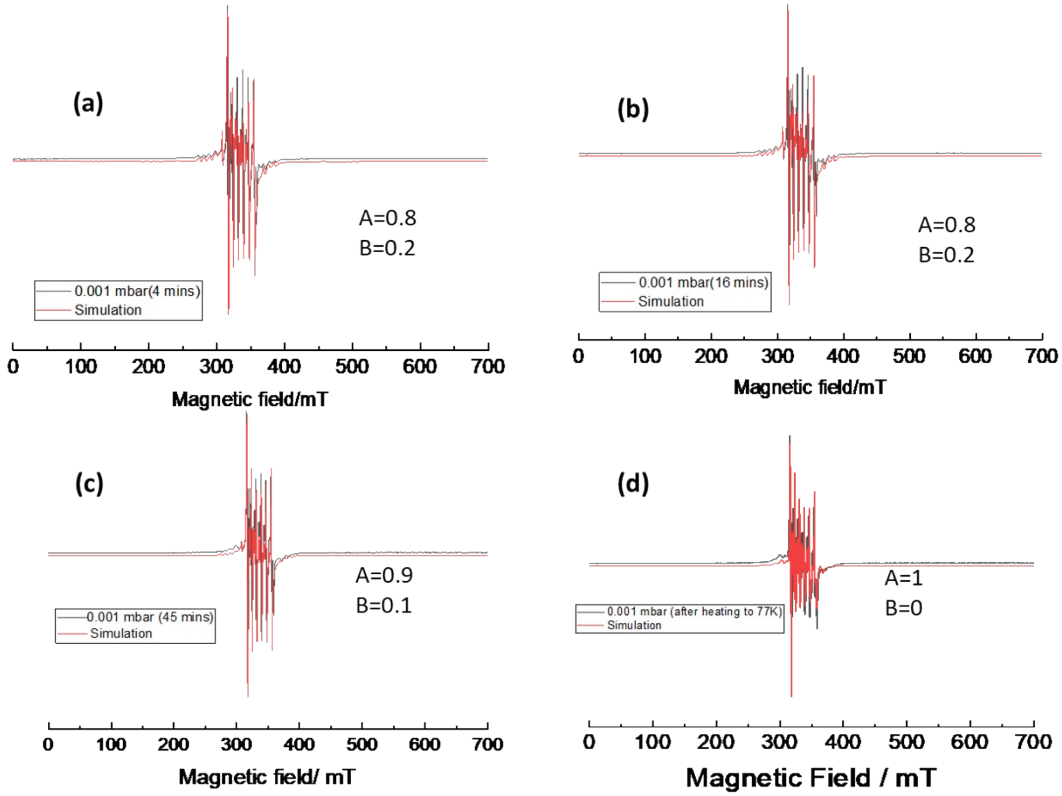


Figure S10. Simulated (red) and experimental (black) *in situ* EPR spectra of Mn-ZIF-8 during $N_2$ desorption, using species A and B, recorded under varying waiting times at pressure 0.001 mbar ($p/p^0$=4.52x10$^{-6}$) mbar and T= 66 K.

*Ex situ* CW EPR measurements were also conducted on $N_2$ adsorbed MN-ZIF-8 at both X-band (Figure S11) and Q-band (Figure S12). For X-band sample preparation, the sample was activated at 150°C for 12 h, followed by exposure to 400 mbar of $N_2$ gas. On the other hand, the Q band sample was activated again at 150°C for 12 h, followed by exposure to 750 mbar of $N_2$ gas.

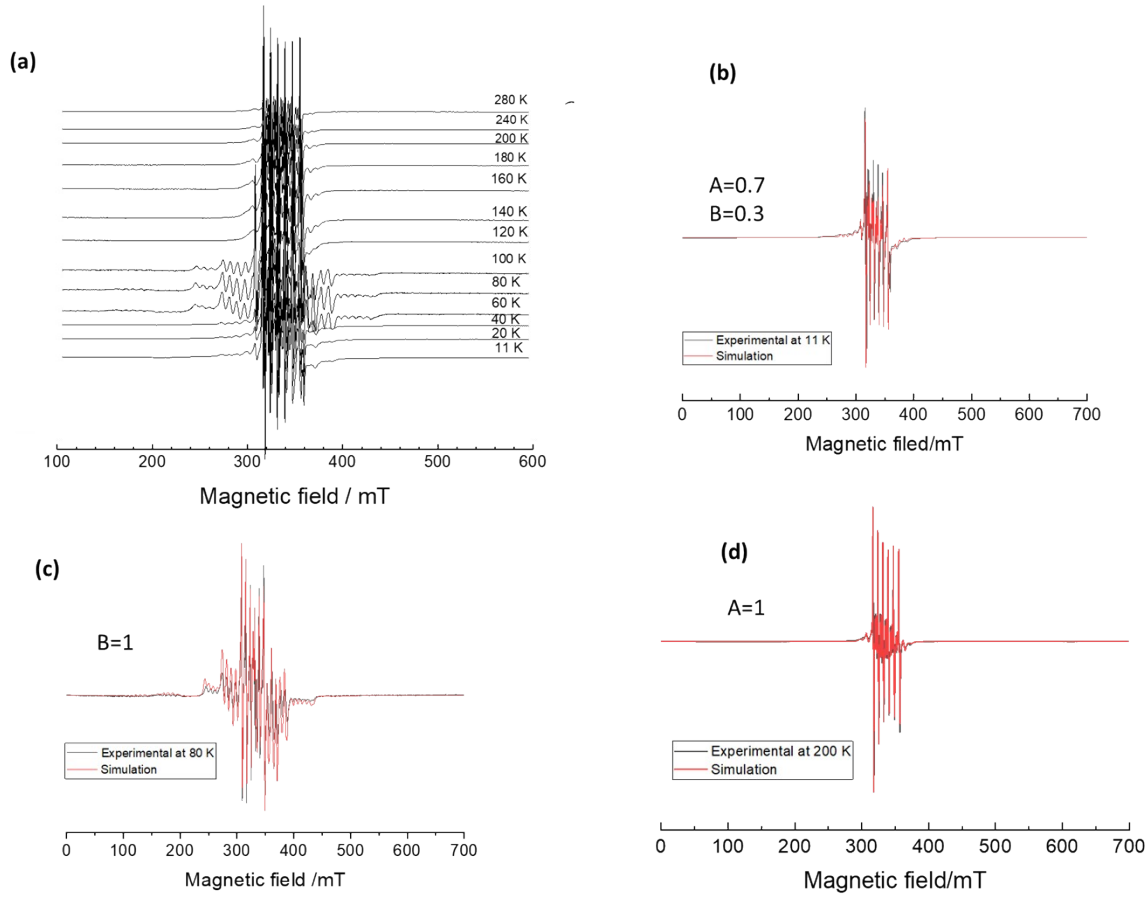


Figure S11. (a) *Ex situ* X-band CW EPR spectra of $N_2$ adsorbed on Mn-ZIF-8. Experimental (black) and simulated(red) X-band *ex situ* EPR spectra at (b) 11 K, (c) 80K and (d) 200 K.

Table S2. Simulated X-band *ex-situ* CW EPR parameters of $N_2$ adsorbed Mn-ZIF-8 at different temperatures.

| Temperature (K) | *g* (MHz) | *A* (MHz) | *D* (MHz) | *E* (MHz) | $B_4^0$(MHz) | $\Delta D$ (MHz) | $\Delta E$ (MHz) |
|---|---|---|---|---|---|---|---|
| 11 (70%Species A) | 2.0005(2) | -217(1) | 350(20) | 20(10) | 0 | 350(10) | 0 |
| 11 (30% Species B) | 2.00002(2) | -217(1) | 1050(10) | 15(0.75) | 0.20(6) | 40(5) | 15(5) |
| 80 (Species B) | 2.00001(2) | -217(1) | 1050(10) | 15(0.75) | 0.20(6) | 40(5) | 15(5) |
| 200 (Species A) | 1.9988(1) | -217(1) | 250(10) | 0 | 0 | 130(5) | 0 |

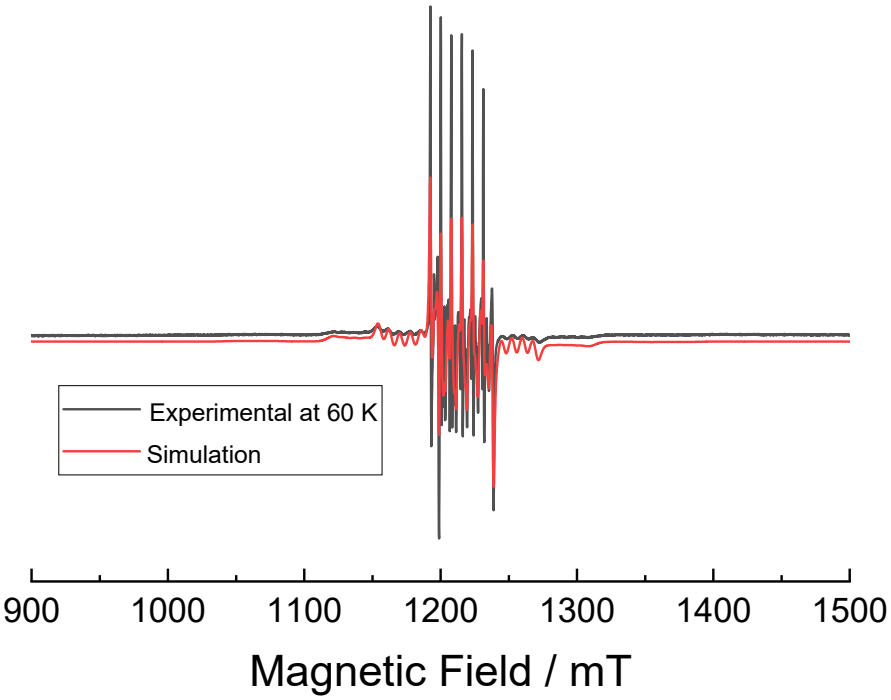


Figure S12. Experimental (black) and simulated (red) Q-band *ex situ* EPR spectra at 60 K. The simulated parameters are exactly the same as that of Species B shown in Table S2.

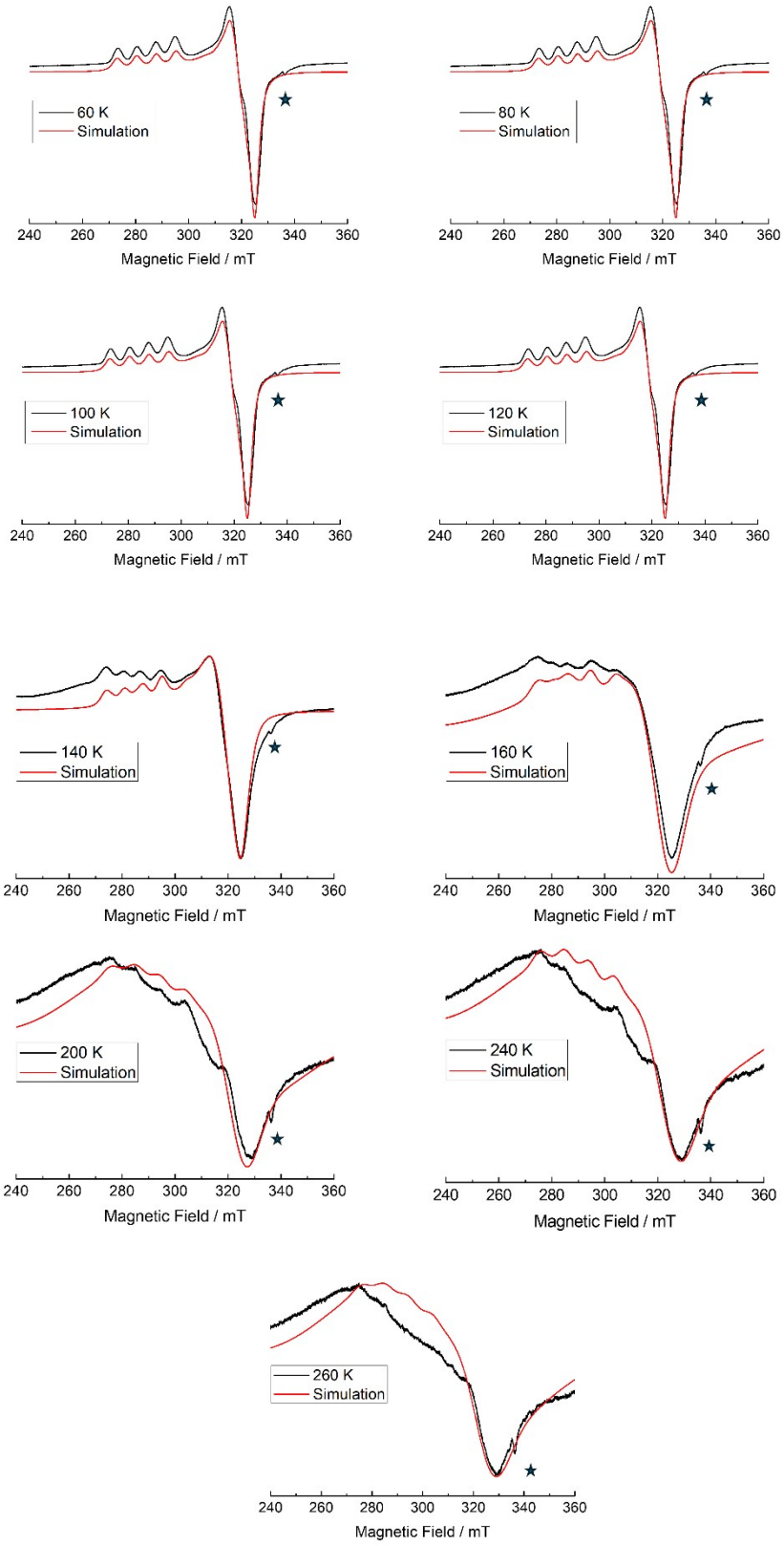


Figure S13a. CW-EPR spectra of the activated Cu-ZIF-8 at variable temperature (black) and their spectral simulations (in red). The signal marked by a star symbol describes the impurity contribution.

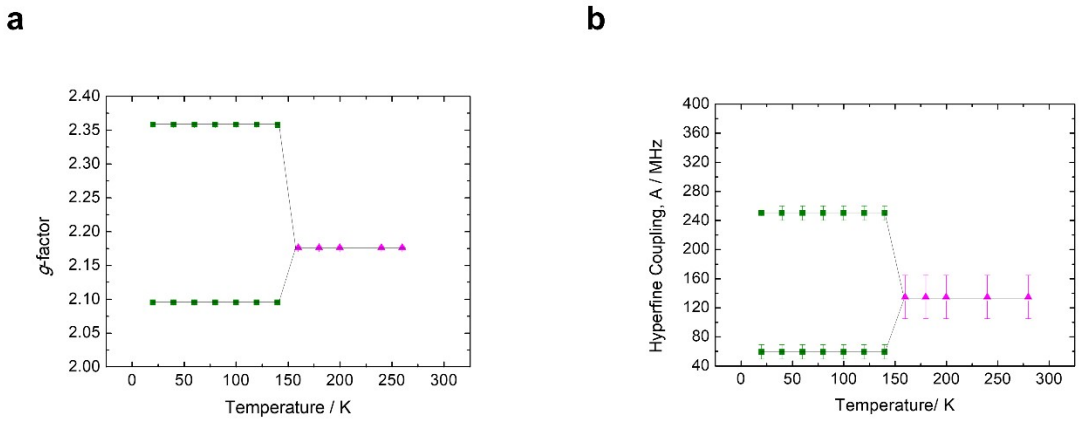


Figure S13b. Plot of EPR parameters of Cu-ZIF-8 obtained via spectral simulation: *g*-factor and hyperfine coupling *A* as a function of measurement temperature. The lines joining the data points is just a guide to the eyes.

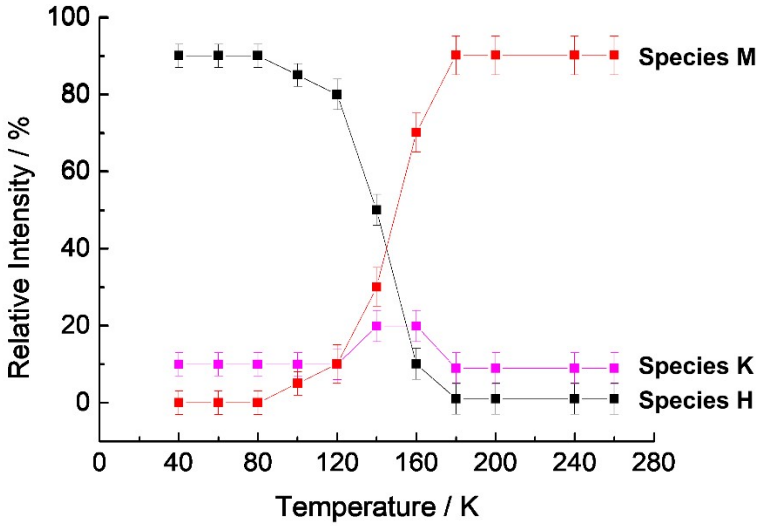


Figure S13c. Plot of molar fraction for species H, K and L obtained from the spectral simulation of CW-EPR spectra of Cu-ZIF-8 at variable temperatures. The lines joining the data points is just a guide to the eyes.

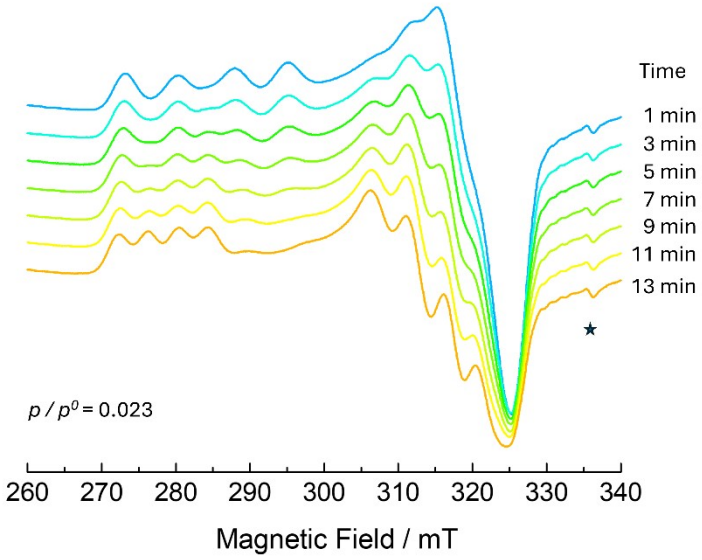


Figure S14. A series of EPR spectra of Cu-ZIF-8 under variation of waiting time was recorded during the adsorption step at $p$ / $p^0$ = 0.023 and 66 K. The signal marked by a star symbol describes the impurity contribution.

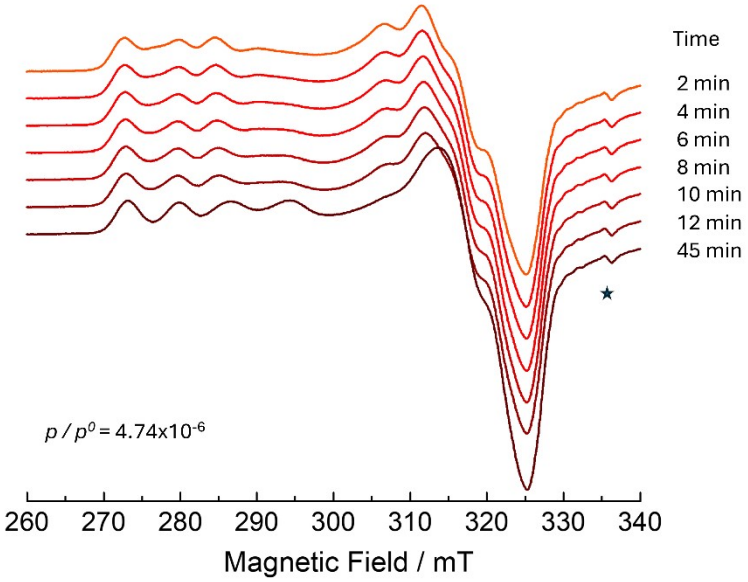


Figure S15. A series of EPR spectra of Cu-ZIF-8 under variation of waiting time was recorded during the desorption step at $p$ / $p^0$ = 4.74x10$^{-6}$ and 66 K. The signal marked by a star symbol describes the impurity contribution.

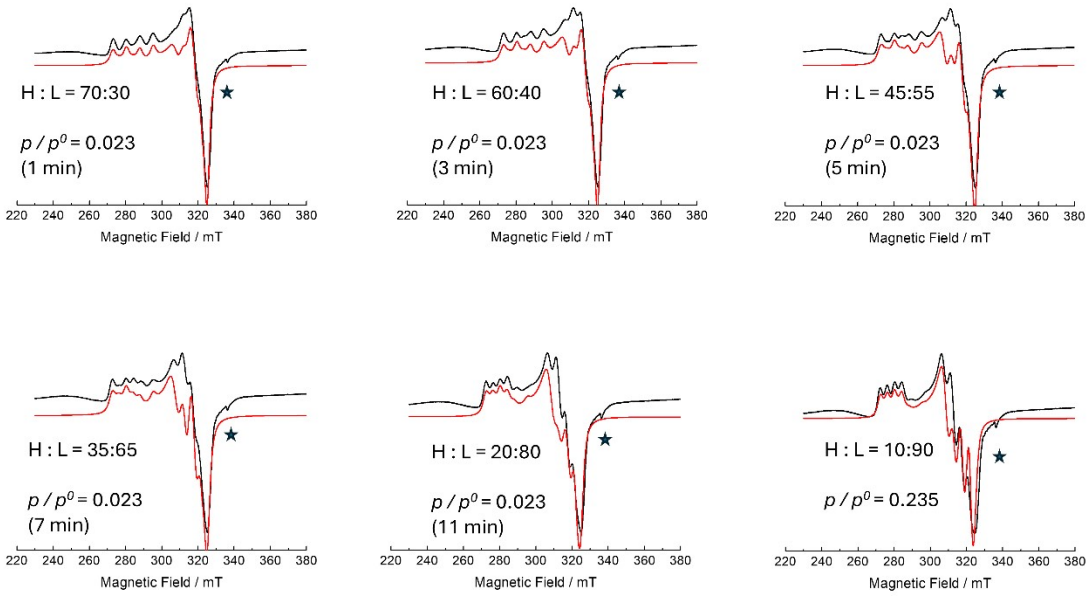


Figure S16. Spectral simulation (red) of selected *in situ* EPR experimental spectra of Cu-ZIF-8 (black). H:L ratio indicates the weighing factor for spectral simulation using species H and L.

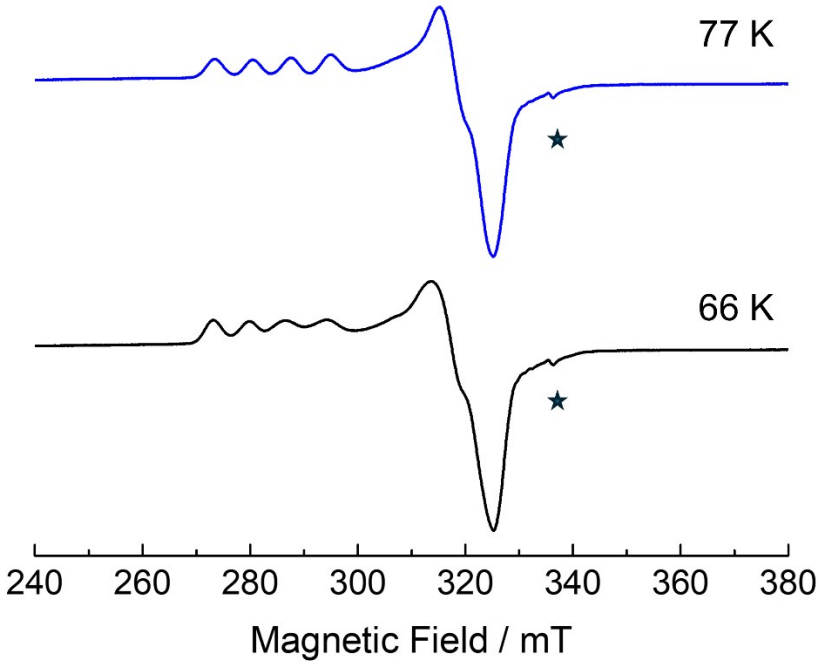

Figure S17. *In situ* EPR spectra of Cu-ZIF-8 during $N_2$ desorption stages (fixed $p$ / $p^0$ = 4.74x10$^{-6}$) measured at two different temperatures. The signal marked by a star symbol describes the impurity contribution.

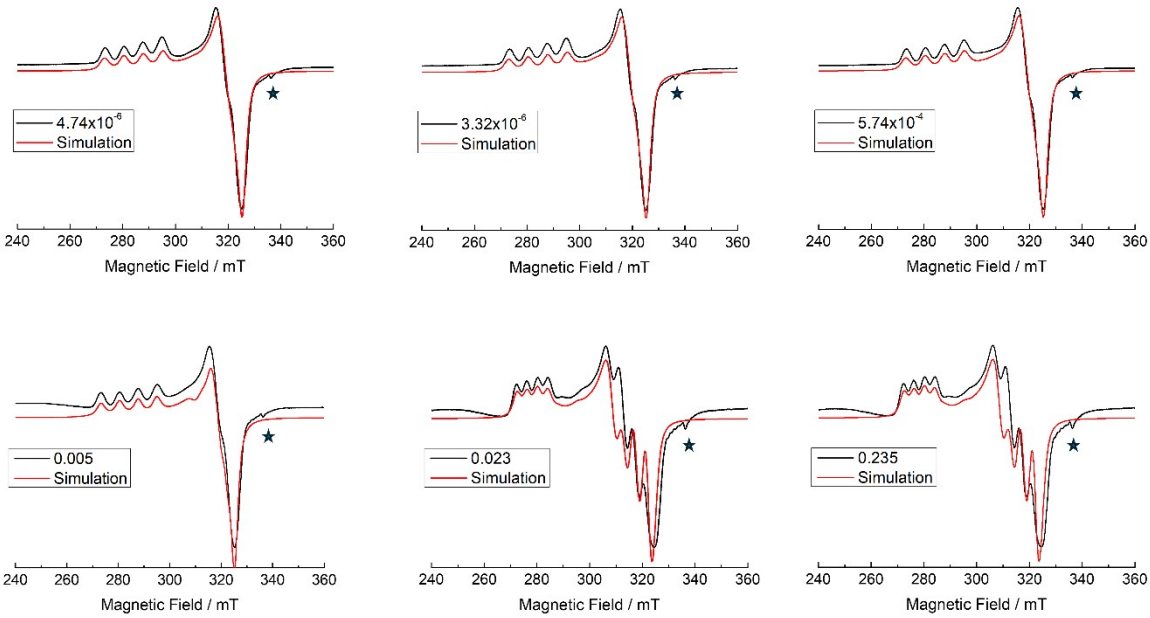


Figure S18. *In situ* EPR spectra of Cu-ZIF-8 during $N_2$ adsorption stages and their corresponding simulation. The signal marked by a star symbol describes the impurity contribution.

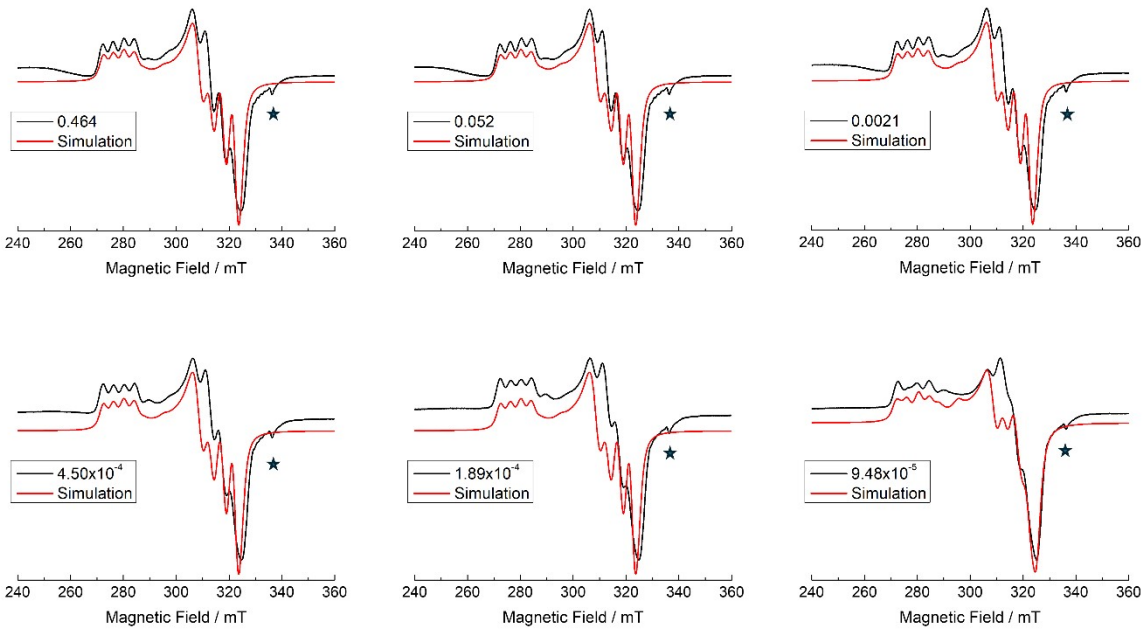

Figure S19. *In situ* EPR spectra of Cu-ZIF-8 during $N_2$ desorption stages and their corresponding simulation. The signal marked by a star symbol describes the impurity contribution.

Table S3. Bonding properties of selected bivalent metal ($M^{2+}$) ions in the ZIF-8 framework.

| Bonding Properties | Zn-N | Mn-N [a] | Cu-N [b] |
|---|---|---|---|
| Bond distance, M-N (Å) | 1.966 | 2.059 | 1.974<br>1.974 |
| Bond Angle, N-M-N (°) | 109.16<br>110.09 | 107.89<br>110.27 | 101.07<br>128.42 |
| References | [4] | [5] | [6] |

[a] Mn-N data is obtained experimentally according to the CIF file reported by Kadota and co-workers [5] .[b] Cu-N data is obtained via DFT calculations of $Cu^{2+}$ ions doped into the ZIF-8 framework.

Table S4. Number *n* of coordinating nitrogen ligands, covalency parameter $\rho$ of $MnN_n$ units, and isotropic hf interaction of $Mn^{2+}$ as derived from the phenomenological relation between *A* and $\rho$ according to references[1,7].

| *n* | $\rho$ *(%)* | A (MHz) |
|---|---|---|
| 3 | 23 | 153 |
| 4 | 17 | 206 |
| 5 | 14 | 228 |
| 6 | 11 | 241 |

# References


1 V. K. Jain and G. Lehmann, *Phys. Status Solidi B*, 1990, *159*, 495–544. doi: 10.1002/pssb.2221590202

2 R. A. Serway, *Phys. Rev. B*, 1971, *3*, 608–615.

3 A. Manoogian, *J. Magn. Reson.*, 1979, *36*, 1–6. doi: 10.1016/0022-2364(79)90210-5.

4 K. S. Park, Z. Ni, A. P. Côté, J. Y. Choi, R. Huang, F. J. Uribe Romo, H. K. Chae, M. O'Keeffe and O. M. Yaghi, *Proc. Natl. Acad. Sci. U. S. A.*, 2006, *103*, 10186–10191. doi: 10.1073/pnas.0602439103

5 K. Kadota, E. Sivaniah, S. Bureekaew, S. Kitagawa and S. Horike, *Inorg. Chem.*, 2017, *56*, 8744–8747. doi: 10.1021/acs.inorgchem.7b01322.

6 M. F. Lukman, P. C. Bruzzese, W. Böhlmann, A. Schnegg and A. Pöppl, *J. Phys. Chem. C*, 2024, *128*, 9130–9141. doi: 10.1021/acs.jpcc.4c01261.

7 E. Šimánek and K. A. Müller, *J. Phys. Chem. Solids*, 1970, *31*, 1027–1040. doi: 10.1016/0022-3697(70)90313-6.